

## MASS DISTRIBUTION IN THE CENTRAL FEW PARSECS OF OUR GALAXY

SEUNGKYUNG OH<sup>1,2</sup>, SUNGSOO S. KIM<sup>1,3,4</sup>, AND DONALD F. FIGER<sup>3</sup>

<sup>1</sup>Dept. of Astronomy & Space Science, Kyung Hee University, Yongin-shi, Kyungki-do 446-701

<sup>2</sup>Argelander-Institute for Astronomy, University of Bonn, Auf dem Huegel 71, 53121 Bonn, Germany

<sup>3</sup>Chester F. Carlson Center for Imaging Science, Rochester Institute of Technology, 54 Lomb Memorial Drive, Rochester, NY 14623-5604, USA

*To appear in the Journal of The Korean Astronomical Society, vol. 42, p. 17 (2009)*

### ABSTRACT

We estimate the enclosed mass profile in the central 10 pc of the Milky Way by analyzing the infrared photometry and the velocity observations of dynamically relaxed stellar population in the Galactic center. HST/NICMOS and Gemini Adaptive Optics images in the archive are used to obtain the number density profile, and proper motion and radial velocity data were compiled from the literature to find the velocity dispersion profile assuming a spherical symmetry and velocity isotropy. From these data, we calculate the enclosed mass and density profiles in the central 10 pc of the Galaxy using the Jeans equation. Our improved estimates can better describe the exact evolution of the molecular clouds and star clusters falling down to the Galactic center, and constrain the star formation history of the inner part of the Galaxy.

*Subject headings:* Galaxy: center — Galaxy: structure — Galaxy: kinematics and dynamics

### 1. INTRODUCTION

The center of the Milky Way is the closest galactic nucleus, at a distance of  $\sim 8$  kpc from the Sun (Ghez et al. 2008; Gillessen et al. 2009), and thus is a good laboratory to study galactic nuclei with. Nonetheless, the Galactic center (GC) had not been studied well enough until 1990s, owing to large interstellar extinction between the GC and the Sun ( $A_V \gtrsim 30$  mag; Rieke, Rieke, & Paul 1989), and the limit in the near-infrared (IR) observing technology in the past. Advances in high-resolution near-IR instruments during the last two decades have yielded a wealth of information on the detailed structure of the GC.

The most central part of the GC harbors a compact massive object, probably a super massive black hole (SMBH) with a mass of  $\sim 4 \times 10^6 M_\odot$  (Ghez et al. 2008; Gillessen et al. 2009). Faint (compared to the stars discussed right below) blue stars known as the “S-stars” or “S-cluster” are observed in the immediate vicinity (within 0.04 pc) of the SMBH. Krabbe et al. (1995) identified them as massive main-sequence stars with a spectral type of B0–B9. Further from the center, between  $\sim 0.04$  and  $\sim 0.4$  pc, a few tens of OB supergiants, giants, and main-sequence stars are observed along with a pool of faint red stars. Paumard et al. (2006) argue that these young stars form two disk-like orbital configurations, highly inclined and rotating counter directions to each other, but note also that Lu et al. (2009) find only one disk.

Kinematical properties of old GC population have been studied as well, although not as intensively as for the young population. Several studies (e.g., Genzel et al. 1996, 2000; Figer et al. 2003) presented and analyzed proper motion and radial velocity observations of the old stellar population. This old population of stars is well relaxed under the influence of SMBH and thus contains some information on the mass distribution and dynamical

environment around the SMBH.

The presence of very young ( $< 10^7$  yr) stars in the central parsec has been a puzzle since the strong tidal forces and magnetic fields in the GC as well as the elevated temperatures in molecular clouds form hostile star formation environment there. Inward migration of a star cluster that is formed far outside the central parsec through dynamical friction has been proposed (Gerhard 2001) to solve this youth paradox, but it was shown that this scenario requires unrealistically extreme initial cluster conditions to explain the observed distribution of young stars in the central parsec (Kim & Morris 2003; Kim, Figer, & Morris 2004). Thus “*in situ*” star formation is a more likely scenario, and star formation through a gravitationally unstable gaseous disk around the SMBH (Nayakshin, Cuadra, & Springel 2007, among others) appears to be the most promising model currently.

The gas material that formed the young stars inside the central parsec had probably come from the farther galactocentric distances, and a ring of dense molecular gas extending 2–7 pc from the SMBH, called a “circumnuclear disk” (CND; Christopher et al. 2005), is a good candidate for its origin. The CND itself shows some evidences of star formation (Yusef-Zadeh et al. 2008) as well.

The initial configuration (e.g., radial and vertical sizes) of the star-forming gaseous disk in the central parsec will depend on the trajectory of the gas material infalling from the CND, which in turn depends on the shape of the gravitational potential in that region (i.e., the central few parsecs). The exact shape of the potential in the central few parsecs will also determine the degree of tidal compression and distortion during the infall of the gas toward the central parsec, which in turn will determine the star formation efficiency in the central parsec.

The masses of the SMBH and its immediate vicinity ( $< 0.1$  pc) have been estimated by analyzing the line-of-sight (LOS) velocities and proper motions of the S-stars (Ghez et al. 2008; Gillessen et al. 2009, among others),

<sup>4</sup> Corresponding author

while the enclosed mass profile (EMP) between 10 and 100 pc from the SMBH has been calculated by analyzing the LOS velocities of the OH/IR stars (Lindqvist, Habing, & Winnberg 1992). The EMP between  $\sim 0.1$  and  $\sim 5$  pc has been studied either by interpreting the velocities of the CNB as those of a rotating, circular ring (Guesten et al. 1987; Jackson et al. 1993; Christopher et al. 2005) or by using the LOS velocity dispersion of old, relaxed stellar population (Genzel et al. 1996, 2000; Figer et al. 2003; Schödel et al. 2007). The estimate from the former sensitively depends on the assumption of a rotating, circular ring, and all of the latter studies are based on the observations only out to  $\sim 0.8$  pc (Genzel et al. 2000 make use of the number count measurement out to  $\sim 5$  pc with the SHARP speckle camera on the 3.5-m New Technology Telescope [NTT] obtained from the diploma thesis of Schmitt 1995, but the quality and reliability of this measurement is difficult to be assessed). Thus the EMP estimate in the central few parsecs regime is still rather uncertain.

In the present paper, we estimate the EMP in this important region, between  $\sim 0.1$  and  $\sim 10$  pc from the GC, by analyzing the *Hubble Space Telescope* (HST) infrared photometry inside the central 5 pc along with the radial velocities and proper motions of the old stellar population in the same region.

## 2. THE DATA

The Jeans equation for a spherically symmetric system will be used in the present study to estimate the EMP in the GC, and for this, one needs number density and velocity dispersion profiles of a relaxed population. The former can be obtained from the stellar photometry, and the latter from the proper motion observations and infrared spectroscopy.

### 2.1. Stellar Photometry

Five near-IR images toward the GC taken with the NICMOS camera 2 (NIC2) onboard the HST, which are available from the HST archive, have been analyzed to obtain the stellar number density profile. We adopted F160W and F222M (similar to Johnson  $H$  and  $K$ ) filter images observed in October 1997 and September 2002. Table 1 lists those image frames, and Figure 1 shows their sizes and locations, which cover the central  $\sim 4$  pc of the GC ( $100''=3.88$  pc at the assumed GC distance of 8 kpc). The five frames are roughly aligned on the Galactic plane, and the two larger frames are mosaiced ones each composed of 4 images. The pixel scale and the field of view of each NIC2 image ( $256 \times 256$  pixels) are  $0.076''/\text{pixel}$  and  $19.2'' \times 19.2''$ , relatively.

We performed PSF photometry using the DAOPHOT package (Stetson 1987) within the Image Reduction and Analysis Facility (IRAF). 7 to 10 bright and relatively isolated stars were used to construct a point-spread function (PSF) of each image. NICMOS PSFs have quite prominent secondary diffraction rings and radial spikes, and automated star-finding algorithms often identify the overlaps of two PSFs as stars. We removed these bogus stars by hand. We assume that the stars have the same intrinsic color  $(m_{F160W} - m_{F222M})_0 = 0.25$  mag (see Kim et al. 2005) and calculate the reddening of each star following an extinction law by Rieke et al. (1989).

The average extinction in our F222M image is found to be  $\sim 3.2$  mag.

We carried out a completeness test by adding artificial stars to the observed images. We find that the 80 % completeness limit of the innermost F222M image is at 14 mag, and use stars brighter than 14 mag for our analyses (the recovery fractions of the F222M images other than the innermost one is greater than 90 % at 14 mag).

Estimation of an EMP requires a density profile of a tracer population that is dynamically relaxed. Most of the stars outside the central 0.4 pc of the GC are intermediate to old populations, while the stars inside 0.4 pc are a mixture of young and older populations (Krabbe et al. 1995). To cull out the young population from the older, we use the CO line strengths from the Adaptive Optics Demonstration Science Data Set of the Gemini telescope.<sup>2</sup> The Gemini GC demo data were observed in July and August 2000 with  $H$ ,  $K'$ ,  $K$ -continuum (centered at  $2.26 \mu\text{m}$  with a bandpass of  $60 \text{ \AA}$ ), and CO (centered at  $2.29 \mu\text{m}$  with a bandpass of  $20 \text{ \AA}$ ) filters. We performed PSF photometry for images 1 (roughly centered at the Sgr A\*) and 2 (centered about  $20''$  away from the Sgr A\*; each image has a field of view of  $20'' \times 20''$ ). We have calibrated the photometry of the two images using the stars that appear on both images, but they are not absolutely calibrated.

Figure 2 shows  $K_{cont}$ -CO vs.  $K_{cont}$  diagrams for stars inside and outside the 0.4 pc radius from the Sgr A\*. Outside 0.4 pc, the color-magnitude diagram forms a relatively narrow stream at the bright end ( $K_{cont} < 16$ ), but inside 0.4 pc, a separate population with redder  $K_{cont}$ -CO colors (i.e., smaller CO absorption strengths) is seen. The small CO strength is an indication of young ages ( $\lesssim 10^7$  yr), and we identify the stars in the box of Figure 2a as the young population. We removed the young stars in the central 0.4 pc from our NICMOS photometry by cross-identifying the Gemini photometry against the NICMOS (the number of young stars was 34 out of 1535 stars with  $F222M < 14$  in our NICMOS photometry). This way, we were able to have a collection of mostly intermediate to old stars that are brighter than 14 mag in  $K'$  in the central 4 pc of the GC, and this sample will be used to produce the density profile of our tracer population.

### 2.2. Stellar Velocities

Genzel et al. (2000) compiled a homogenized data set of stellar velocities within the central 0.8 pc of the GC by combining various proper motion and LOS velocity data from the New Technology Telescope (NTT), the Keck telescope, and the MPG/ESO telescope on La Silla. Figer et al. (2003) reported LOS velocities of 85 cool stars in the central parsec of the GC obtained with the Keck telescope.<sup>3</sup> We combined these two data sets to create a larger velocity sample of late-type (old) stars in the central parsec. 49 stars appear on both data sets, and we adopted the radial velocities from the Keck for those

<sup>2</sup> Available at [http://gemini.conicyt.cl/sciops/data/release\\_doc/manual.html](http://gemini.conicyt.cl/sciops/data/release_doc/manual.html)

<sup>3</sup> Zhu et al. (2008) report the second epoch observations of the LOS velocities toward the same region with the same telescope, which mainly target the accelerations of the stars. The velocity data from the second epoch are very similar to the first epoch, i.e., Figer et al. (2003).

common stars. The total numbers of late-type stars in this sample are 80 for the proper motion data and 236 for the LOS velocity data.

Although not as much as found for young stars, old stars in the GC show some figure rotation as well. Following Genzel et al. (1996), we have subtracted a rotational velocity of

$$v_{rot,z} = 24(\Delta l/5'')^{0.4} \text{ km/s} \quad (1)$$

from our LOS velocities ( $\Delta l$  is the Galactic longitude offset from Sgr A\*).

The stars in this data set extend out only to  $\sim 0.8$  pc from the Sgr A\*, we add to this data set two LOS velocity dispersion values at  $\sim 1.3$  pc and  $\sim 4$  pc that Genzel et al. (1996) have obtained from the literature (see their Table 6).

### 3. NUMBER DENSITY PROFILES

Our photometry gives a distribution of projected stellar distances from Sgr A\* ( $R$ ) for the tracer population in the central 4 pc region, and the surface number density profile ( $\Sigma[R]$ ) obtained from this distribution is shown with asterisks in Figure 3. To obtain a spatial number density profile ( $n[r]$ ;  $r$  is the spatial radius from Sgr A\*) from  $\Sigma(R)$ , we model  $n(r)$  with three functional forms adopted in previous studies.

Genzel et al. (1996) implemented the following functional form for the spatial density:

$$n(r) = \frac{\Sigma_0}{r_0} \frac{1}{1 + (r/r_0)^\alpha}. \quad (2)$$

Here,  $\Sigma_0$ ,  $r_0$ , and  $\alpha$  are the parameters to be found. The information directly available from observations is  $\Sigma(R)$ , and  $n(r)$  can be transformed into  $\Sigma(R)$  by the Abel integral equation,

$$\Sigma(R) = 2 \int_R^\infty \frac{n(r)}{\sqrt{r^2 - R^2}} r dr. \quad (3)$$

We numerically integrate this equation when fitting our  $\Sigma(R)$  data from the observations. Genzel et al. (1996) fixed  $\alpha$  to be an asymptotic value at large  $r$ , 1.8, but here we keep it as a free parameter. This density model will be designated as G96.

Saha, Bicknell, & McGregor (1996) modeled the surface density with

$$\Sigma(R) = \Sigma_0 \left( 1 + \frac{R^2}{R_0^2} \right)^{-\alpha}, \quad (4)$$

where  $\Sigma_0$  and  $R_0$  are to be fitted. This model is a variant of the modified Hubble law for elliptical galaxies, and has an analytical counterpart for the spatial density of

$$n(r) = \frac{\Sigma_0}{R_0 B(1/2, \alpha)} \left( 1 + \frac{r^2}{R_0^2} \right)^{-(\alpha+1/2)}, \quad (5)$$

where  $B$  is the beta function. Saha et al. (1996) constrained  $\alpha$  to be 0.4, but we leave it as a free parameter. This model will be called S96.

Alexander (1999) adopted a broken power-law spatial density model:

$$n(r) = \begin{cases} n_0 (r/r_0)^{-\alpha} & r < r_0 \\ n_0 (r/r_0)^{-\beta} & r \geq r_0, \beta > 1 \end{cases}, \quad (6)$$

where  $n_0$ ,  $r_0$ ,  $\alpha$ , and  $\beta$  are the parameters to be fitted. Alexander (1999) assumed  $r_0 = 0.4$  pc ( $10''$ ) and  $\beta = 1.8$  for his fits, but again, we keep them as free parameters. We call this model A99.

When fitting the above functions to our NICMOS data, we try both  $\chi^2$  test and Kolmogorov-Smirnov (KS) test (see, e.g., Press et al. 1992 for the latter).  $\chi^2$  test is widely used as a standard statistical method for comparing two distributions, but its result becomes sensitive on the choice of the number and ranges of the bins if the number of incidences in some of the bins is too small (say, less than  $\sim 10$ ). Since the number of intermediate to old stars in our data sample is small at the very vicinity of the GC ( $R < 5''$ ), this may make the  $\chi^2$  test somewhat unreliable. For this reason, we also use the KS test as a supplementary test. KS test utilizes the cumulative distribution function instead of the histogram, and does not suffer the arbitrariness problem. Note that, however, KS test has its own shortcoming, and this will be discussed shortly.

Figure 3 shows our best  $\chi^2$  and KS fits of the above density models to NICMOS data (Table 2 lists our best-fit density model parameters). The  $\chi^2$  fits show a good agreement between different density models although the innermost bin appears to be slightly over-fitted. The probabilities that the model has a different distribution from the observation are less than 2 % for all three models, so the slight over-fit in the innermost bin is statistically not important.

The KS test results in similar fits for models S96 and A99, but it gives a rather large discrepancy at the innermost bin for model G96. This is probably because (normalized) cumulative distribution functions always start with 0 and end with 1, making the KS test rather insensitive at both ends of the distribution. Model G96 is the least flexible function near the core radius ( $r_0$ ), so it finds a bit difficult to adapt itself to a sudden change near the core radius seen in the observation. Nonetheless, all three KS fits are consistent with the observation by better than 98 % just as in  $\chi^2$  tests.

We do not choose the best density model out of these six fits at this point. Instead, we will see how much difference is made to the final EMP estimates from these six models.

Note that all of our best-fits give  $n \propto r^{-1.5}$  or similar relations at large  $r$ . This is somewhat shallower than those by Schödel et al. (2007;  $r^{-1.75}$ ) and by Genzel et al. (2000;  $r^{-1.8}$ ). These previous estimates are based on the photometry with less sensitivity and/or smaller radii covered than in the present study, and this is thought to be the cause of such differences.

### 4. VELOCITY DISPERSION PROFILE

The radii of the stars with proper motion data in our sample range from  $\sim 0.05$  to  $\sim 0.5$  pc, and those with the LOS velocity data range from  $\sim 0.1$  to  $\sim 5$  pc. Thus our projected tangential and projected radial velocity dispersions ( $\sigma_T$  and  $\sigma_R$ , respectively) from the proper motion data only cover the deepest region, and our LOS velocity dispersion ( $\sigma_z$ ) covers much wider region except the innermost area. These dispersion profiles are shown with three different symbols in Figure 4.

For a functional form of spatial (i.e., not projected) velocity dispersion ( $\sigma_v$ ), we adopt the following parame-

terization used by Genzel et al. (1996):

$$\sigma_v(r)^2 = \sigma_\infty^2 + \sigma_0^2 (r/r_{0v})^{-\gamma}. \quad (7)$$

For  $r_{0v}$ , we use the same  $r_0$  or  $R_0$  of the density model that is used to fit the above equation to the observed velocity dispersions (see below). Thus only  $\sigma_\infty$ ,  $\sigma_0$ , and  $\gamma$  are the parameters to be found.

We assume that the velocity distribution is isotropic. We do not try anisotropic velocity models in the present paper because the spatial coverages of our proper motion sample and LOS velocity sample overlap only marginally.

Since we assume an isotropy for the velocity dispersion, the relation between the observed velocity dispersion and the spatial velocity dispersion is given by

$$\sigma_T(R)^2 = \sigma_R(R)^2 = \sigma_z(R)^2 = \frac{2}{\Sigma(R)} \int_R^\infty \frac{n(r)\sigma_v(r)^2}{\sqrt{r^2 - R^2}} r \, \mathfrak{B} \quad (8)$$

Thus obtaining a functional form for  $\sigma_v(r)$  profile requires spatial and surface density profile information, and we try all of our six fits for  $\Sigma(R)$  (and its corresponding  $n[r]$ ) obtained in the previous section. Figure 4 plots our model (eq. 8) fits to the observed velocity dispersions with three different density profiles (G96, S96, and A99) and two different statistical tests ( $\chi^2$  and KS). All six fits result in very similar velocity dispersion profiles (best-fit velocity dispersion parameters are listed in Table 3).

## 5. ENCLOSED MASS PROFILE IN THE GALACTIC CENTER

The Jeans equation is the first moment of the collisionless Boltzmann equation, and it gives a relation between the enclosed mass of a system and the velocity dispersions. For a spherically symmetric, rotating system with an isotropic velocity distribution, the equation becomes

$$\frac{GM(r)}{r} = v_{rot}(r)^2 + \sigma_v(r)^2 \left\{ -\frac{d \ln[n(r)]}{d \ln r} - \frac{d \ln[\sigma_v(r)^2]}{d \ln r} \right\}, \quad (9)$$

where  $M$  is the enclosed mass and  $v_{rot}$  is the rotational velocity. The latter as a function of  $r$  can be obtained from the observed, mean LOS velocities as a function of the longitude offset from Sgr A\* by the following relation:  $v_{rot,z}(\Delta l)$ :

$$v_{rot}(r) = -\frac{r}{\pi n(r)} \int_r^\infty \frac{d}{d\Delta l} \left( \frac{\Sigma(\Delta l)v_{rot,z}(\Delta l)}{\Delta l} \right) \frac{d\Delta l}{\sqrt{\Delta l^2 - r^2}}. \quad (10)$$

For the density profile in this Abel transform, we use the density model for old population in Genzel et al. (1996) instead of those obtained in the present study because it better represents the whole inner bulge (several tens to hundreds of parsecs) in which the figure rotation takes place.

Figure 5a shows the EMPs obtained from the above Jeans equation with our density and velocity dispersion fits for the intermediate to old stellar populations. These profiles are quite similar to each other, but quite different from the two previous studies, Genzel et al. (2000) and Schödel et al. (2007). Our EMP is similar to the former at larger radii but is considerably larger than the former. The latter has much smaller EMP in the larger

radii because it is based on a rather simple approximation that the LOS velocity dispersion in the outer region is constant.

We do not plot our EMPs inside 0.2 pc. Our EMP estimates at this inner region are not reliable because there are not many bright, intermediate to old stars in this region (this “hole” of old stars is probably due to frequent close encounters with other stars; see Genzel et al. 1996).

For a smooth convergence of the EMP to the mass of the SMBH, we extrapolate the EMP inward from the radius at  $M = 5 \times 10^6 M_\odot$  assuming that the extended mass (the mass excluding the SMBH) distribution follows a power-law function and that the mass of the SMBH is  $4 \times 10^6 M_\odot$  (Ghez et al. 2008; Gillessen et al. 2009). Figure 5b (and Table 4) shows such inward extrapolation of our  $\chi^2$  best-fit of A99 density model (A99/ $\chi^2$ ). We choose this model as our canonical fit as it describes the observed density profile the best and its EMP roughly represents the average of all our 6 models.

Local densities of the extended mass (the mass other than the SMBH) can be obtained by differentiating the EMP. The density profile for our A99/ $\chi^2$  model is given in Figure 6 and Table 4. Again, our result is quite close to that of Genzel et al. at larger radii, but closer to that of Schödel et al. at smaller radii.

## 6. SUMMARY AND DISCUSSION

We have estimated the EMP in the central 10 pc of the Milky Way by analyzing the infrared photometry and the velocity observations of dynamically relaxed stellar population in the Galactic center. HST/NICMOS and Gemini images were used to obtain the number density profile of the relaxed population, and the LOS velocities and proper motion data of the same population were used to calculate the EMP from the Jeans equation assuming a spherical symmetry and velocity isotropy. The newly obtained EMP is larger than the previous studies at  $0.1 < r < 10$  pc, which is consistent with the most recent value for the mass of the SMBH.

As discussed in §1, the enclosed mass and density profiles in the central few parsecs will determine the exact morphological evolution of the molecular clouds and star clusters that are moving down to the GC. Our larger EMP implies that star clusters and molecular clouds in the central few parsecs will have smaller tidal radii and shorter orbital periods than previously expected.

Degenerate stellar remnants such as stellar mass black holes and neutron stars are thought to be segregated in the GC due to their gradual dynamical friction with lighter field stars (Morris 1993). Our density profile can be used to constrain the amount of segregated degenerate objects. Since the current reservoir of degenerate stars is a result of continuous star formation in the GC (Figer et al. 2004), a detailed study on the stellar populations in the GC based on our EMP estimate will constrain the star formation history in the GC as well.

The anonymous referee suggested density profile functions that have an inner radial cutoff to better describe the “hole” of old stars. We do not try such functions here because they will not significantly change our results on the EMP and the nature of the hole is beyond the scope of the present paper, but we do believe that such functions can give some constraints on the size of

the hole.

This work was supported by the 2009 Sabbatical Leave program of Kyung Hee University. S. O. was supported by the Astrophysical Research Center for the Structure and Evolution of the Cosmos (ARCSEC) of the Korea Science and Engineering Foundation through the Sci-

ence Research Center (SRC) program. The material in this paper is partially supported by NASA under award NNG 05-GC37G, through the Long Term Space Astrophysics program. The research by D. F. F. was performed in the Rochester Imaging Detector Laboratory with support from a NYSTAR Faculty Development Program grant.)

#### REFERENCES

- Alexander, T. 1999, *ApJ*, 527, 835  
 Christopher, M. H., Scoville, N. Z., Stolovy, S. R., & Yun, M. S. 2005, *ApJ*, 622, 346  
 Figer, D. F., et al. 2003, *ApJ*, 599, 1139  
 Figer, D. F., Rich, R. M., Kim, S. S., Morris, M., & Serabyn, E. 2004, *ApJ*, 601, 319  
 Gerhard, O. 2001, *ApJ*, 546, L39  
 Ghez, A. M., et al. 2008, *ApJ*, 689, 1044  
 Genzel, R., Thatte, N., Krabbe, A., Kroker, H., & Tacconi-Garman, L. E. 1996, *ApJ*, 472, 153  
 Genzel, R., Pichon, C., Eckart, A., Gerhard, O. E., & Ott, T. 2000, *MNRAS*, 317, 348  
 Gillessen, S., Eisenhauer, F., Trippe, S., Alexander, T., Genzel, R., Martins, F., Ott, T. 2009, *ApJ*, in press  
 Guesten, R., et al. 1987, *ApJ*, 318, 124  
 Jackson, J. M., et al. 1993, *ApJ*, 402, 173  
 Kim, S. S., & Morris, M. 2003, *ApJ*, 597, 312  
 Kim, S. S., Figer, D. F., & Morris, M. 2004, *ApJ*, 607, L123  
 Kim, S. S., Figer, D. F., Lee, M. G., & Oh, S. 2005, *PASP*, 117, 445  
 Krabbe, A., et al. 1995, 447, L95  
 Lindqvist, M., Habing, H. J., & Winnberg, A. 1992, *A&A*, 259, 118  
 Lu, J. R., Ghez, A. M., Hornstein, S. D., Morris, M. R., Becklin, E. E., & Matthews, K. 2009, *ApJ*, 690, 1463L  
 Morris, M. 1993, *ApJ*, 408, 496  
 Nayakshin, S., Cuadra, J., & Springel, V. 2007, *MNRAS*, 379, 21  
 Paumard, T., et al. 2006, *ApJ*, 643, 1011  
 Press, W. H., Teukolsky, S. A., Vetterling, W. T., & Flannery, B. P. 1992, *Numerical Recipes in FORTRAN. The Art of Scientific Computing*, 2nd (Cambridge: Univ. Press)  
 Rieke, G. H., Rieke, M. J., & Paul, A. E. 1989, *ApJ*, 336, 752  
 Saha, P., Bicknell, G. V., & McGregor, P. J. 1996, *ApJ*, 467, 636  
 Schmitt, J. 1995, Diploma thesis, Ludwig-Maximilian University, Munich  
 Schödel, R., et al. 2007, *A&A*, 469, 125  
 Stetson, P. 1987, *PASP*, 99, 191  
 Yusef-Zadeh, F., Braatz, J., & Wardle, M., & Roberts, D. 2008, *ApJ*, 683, L147  
 Zhu, Q., Kudritzki, R. P., Figer, D. F., Najarro, F., & Merritt, D. 2008, *ApJ*, 681, 1254

TABLE 1  
HST/NICMOS DATASETS ANALYZED IN THE PRESENT  
STUDY

Dataset Name	Exposure (Sec)	Observation Date
F160W		
N49Z010H0	25.9	October 1997
N49Z01030	55.9	October 1997
N49Z01070	55.9	October 1997
N49Z010B0	55.9	October 1997
N49Z010F0	55.9	October 1997
N49Z02030	55.9	October 1997
N49Z02070	55.9	October 1997
N49Z020B0	55.9	October 1997
N49Z020F0	55.9	October 1997
N6LO02050	24.0	September 2002
N6LO03050	24.0	September 2002
F222M		
N49Z010I0	71.9	October 1997
N49Z01040	207.9	October 1997
N49Z01080	207.9	October 1997
N49Z010C0	207.9	October 1997
N49Z010G0	207.9	October 1997
N49Z02040	207.9	October 1997
N49Z02080	207.9	October 1997
N49Z020C0	207.9	October 1997
N49Z020G0	207.9	October 1997
N6LO02040	71.9	September 2002
N6LO03040	71.9	September 2002

TABLE 2  
SURFACE NUMBER DENSITY FITS

G96		S96		A99		G96		S96		A99	
$\chi^2$ Fit						KS Fit					
$\Sigma_0$	247	$\Sigma_0$	1130	$n_0$	994.7	$\Sigma_0$	343	$\Sigma_0$	1100	$n_0$	1168.1
$r_0$	0.11	$R_0$	0.13	$r_0$	0.17	$r_0$	0.44	$R_0$	0.14	$r_0$	0.15
$\alpha$	1.50	$\alpha$	0.25	$\alpha$	0.45	$\alpha$	1.48	$\alpha$	0.25	$\alpha$	0.59
				$\beta$	1.47					$\beta$	1.48

NOTE. —  $\Sigma_0$  are in units of  $\text{pc}^{-2}$ ,  $n_0$  in  $\text{pc}^{-3}$ , and  $r_0$  &  $R_0$  in pc.

TABLE 3  
VELOCITY DISPERSION PROFILE FITS

	G96	S96	A99	G96	S96	A99
	$\chi^2$ Fit			KS Fit		
$\sigma_\infty$	30.9	31.3	28.1	44.9	44.8	38.0
$\sigma_0$	253	237	209	170	201	210
$\gamma$	0.77	0.77	0.73	1.11	0.99	0.81

NOTE. —  $\sigma_\infty$  and  $\sigma_0$  values are in units of km/s.

TABLE 4  
ENCLOSED MASS AND DENSITY  
PROFILES IN THE GALACTIC  
CENTER

$r$ (pc)	$M$ ( $M_{\odot}$ )	$\rho$ ( $M_{\odot}/\text{pc}^3$ )
0.1	4.15e+06	2.49e+07
0.2	4.40e+06	5.87e+06
0.3	4.73e+06	3.25e+06
0.5	5.54e+06	1.33e+06
0.7	6.33e+06	6.30e+05
1.0	7.47e+06	3.04e+05
2.0	1.16e+07	8.88e+04
3.0	1.65e+07	4.76e+04
5.0	2.90e+07	2.29e+04
7.0	4.48e+07	1.42e+04

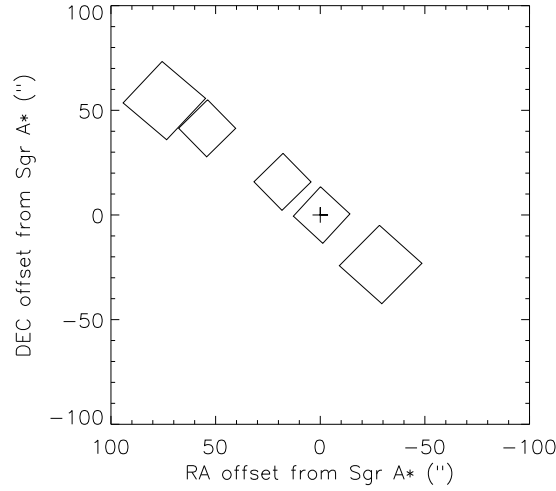


FIG. 1.— Locations and sizes of the *HST*/NICMOS images used in the present study. The cross at the center indicates the Sgr A\*. The five frames are roughly aligned along the Galactic plane, and the two larger frames are mosaiced ones each composed of 4 images.

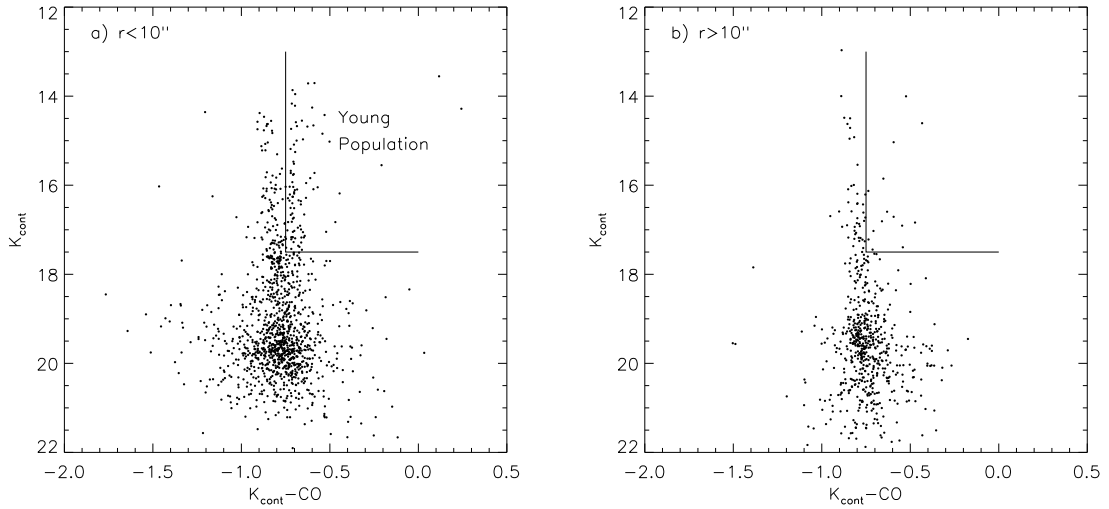


FIG. 2.—  $K_{cont}-CO$  vs.  $K_{cont}$  diagrams for the stars in  $r < 10''$  (a) and  $r > 10''$  (b) regions from the Gemini Adaptive Optics data. The magnitudes presented here are not calibrated ones (we find that our Gemini  $K_{cont}$  magnitudes are  $\sim 3.6$  mag fainter than the NICMOS F222M magnitudes on average). A separate population of stars is seen in the area defined by  $K_{cont} - CO > -0.75$  and  $K_{cont} < 17.5$  (denoted with the straight lines) at  $r < 10''$ . This population is mostly composed of young stars (see the text).



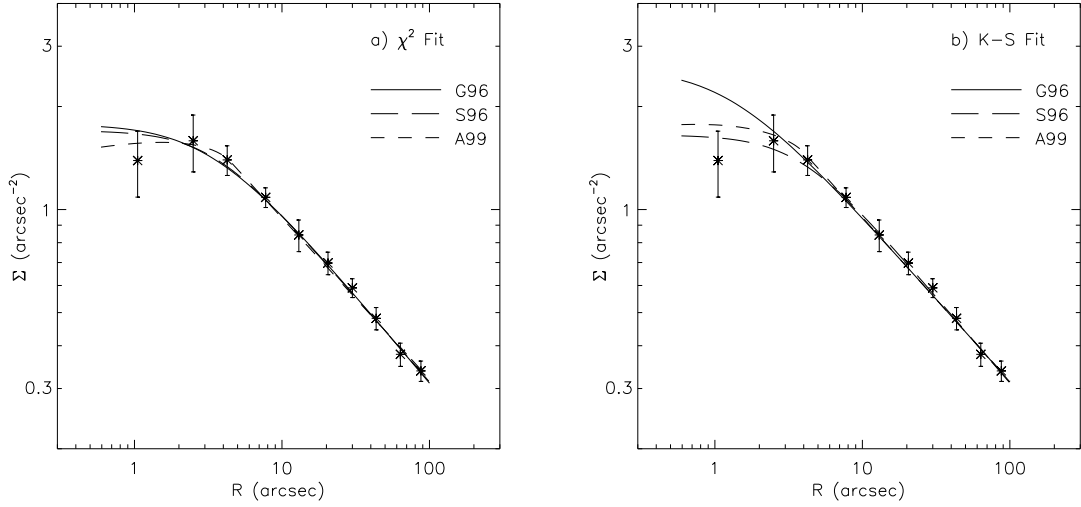


FIG. 3.— Best-fit surface density profiles for density models of Genzel et al. (1996; G96), Saha et al (1996; S96), and Alexander (1997; A99) using the  $\chi^2$  test (a) and the Kolmogorov-Smirnov test (b). The surface densities from our analysis of HST/NICMOS images (after the subtraction of young population) are shown with asterisks and  $1\text{-}\sigma$  error bars.

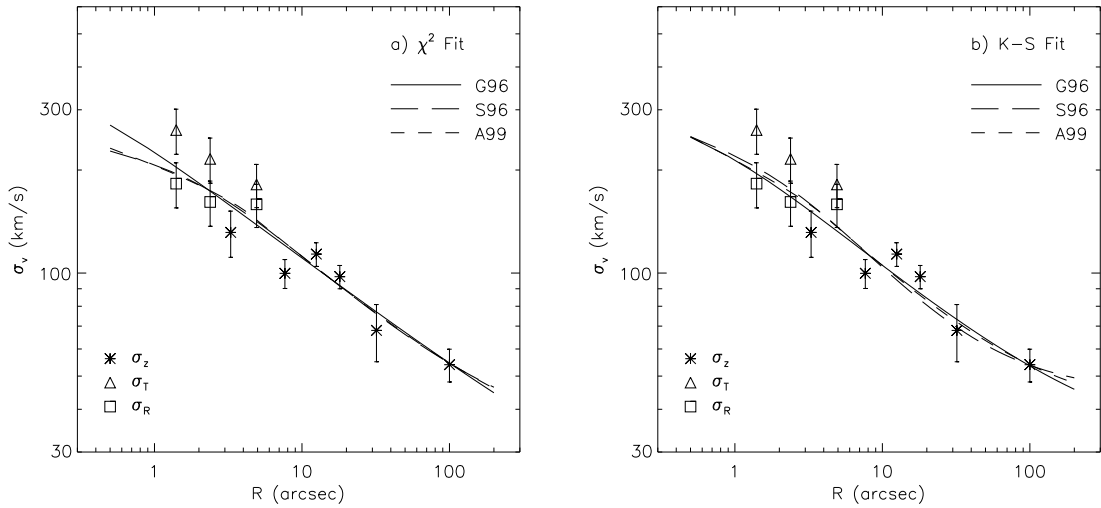


FIG. 4.— Best-fit velocity dispersion profiles for density models of Genzel et al. (1996; G96), Saha et al (1996; S96), and Alexander (1997; A99) using the  $\chi^2$  test (a) and the Kolmogorov-Smirnov test (b). The velocity dispersion data, which we obtained from Genzel et al. (1996, 2000) and Figer et al. (2003), are shown with symbols and  $1\text{-}\sigma$  error bars.

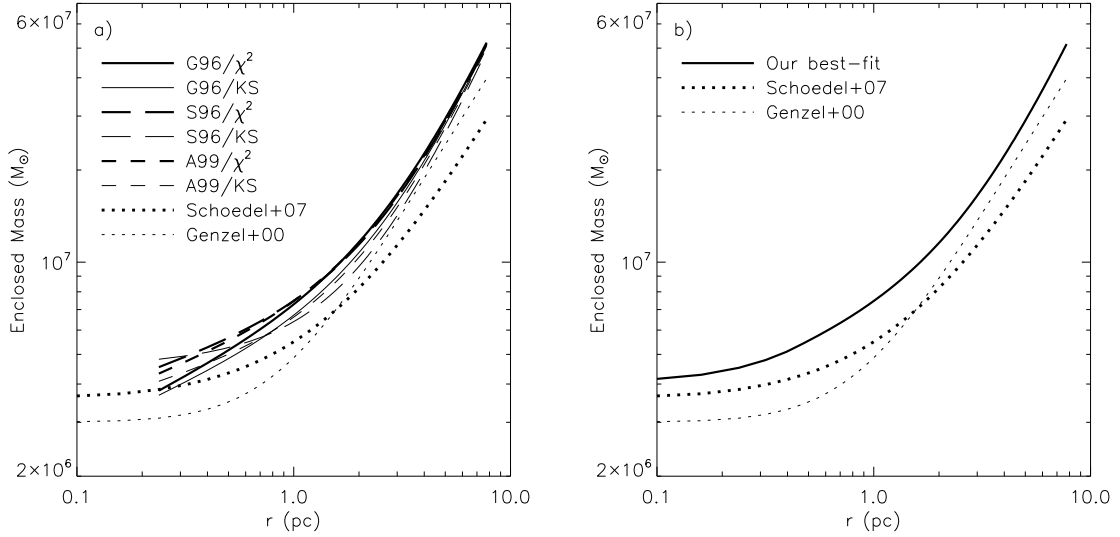


FIG. 5.— (a) Enclosed mass profiles from the Jeans equation for density models of Genzel et al. (1996; G96), Saha et al (1996; S96), and Alexander (1999; A99) and statistical tests of  $\chi^2$  and Kolmogorov-Smirnov (KS) methods. (b) Enclosed mass profile of A99/ $\chi^2$  model modified to converge to the SMBH mass of  $4 \times 10^6 M_{\odot}$  at  $r = 0$  pc (our best-fit). Also plotted are the enclosed mass profiles estimated by Schödel et al. (2007) and Genzel et al. (2000).

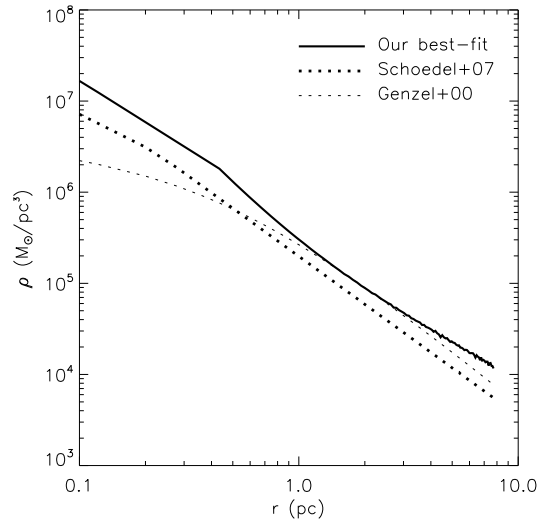


FIG. 6.— Density profile of the modified A99/ $\chi^2$  model (our best-fit; see Fig. 5b) along with those estimated by Schödel et al. (2007) and Genzel et al. (2000).